



Cite this: *Dalton Trans.*, 2015, **44**, 1186

$\text{La}_{1-x}\text{Ln}_x\text{H}(\text{O}_3\text{PCH}_3)_2$ ($\text{Ln} = \text{Tb}, \text{Eu}; 0 < x \leq 1$): an organic–inorganic hybrid with lanthanide chains and tunable luminescence properties†

B. Mutelet,^a S. Boudin,^{*a} O. Pérez,^a J. M. Rueff,^a C. Labbé^b and P. A. Jaffrès^c

The organic/inorganic $\text{La}_{1-x}\text{Ln}_x\text{H}(\text{O}_3\text{PCH}_3)_2$ ($\text{Ln} = \text{Eu}, \text{Tb}$) hybrids have been synthesized by hydrothermal synthesis. The crystal structure of $\text{LaH}(\text{O}_3\text{PCH}_3)_2$ consists of chains of edge-sharing LaO_8 polyhedra linked through PO_3C tetrahedra. Photoluminescence of Eu^{3+} , Tb^{3+} and $\text{Eu}^{3+}/\text{Tb}^{3+}$ co-doped materials have been investigated. The Eu and Tb hybrids show no concentration quenching versus doping rate suggesting energy migration through a percolation model. The Eu hybrids exhibit a red emission while the Tb ones exhibit, with the Tb rate increasing, a blue to green emission under a 378 nm excitation wavelength and a cyan to green emission under a 262 nm excitation wavelength. The doping rate dependent red shift results from a cross relaxation phenomenon between closed Tb^{3+} ions. The blue to cyan shift observed for the slightly doped materials, when excitation wavelength shifts from 378 nm to 262 nm, is due to different relaxation phenomena, from the $^5\text{D}_3$ level for a 378 nm excitation wavelength and from the $^5\text{D}_4$ level via the 4f5d level for a 262 nm excitation wavelength. Under a 378 nm wavelength, the co-doped $\text{La}_{0.93}\text{Eu}_{0.03}\text{Tb}_{0.04}\text{H}(\text{O}_3\text{PCH}_3)_2$ hybrid exhibits a white/cyan emission with CIE coordinates equal to $x = 0.29$, $y = 0.37$.

Received 29th August 2014,
Accepted 1st November 2014

DOI: 10.1039/c4dt02643h

www.rsc.org/dalton

1 Introduction

Metal phosphonates have been extensively studied in the last few decades due to their large potential applications as molecular sieves, ions exchangers, sorbents, catalysts, proton conductors, opto-electronics and non-linear optical materials.^{1–6} Among those materials, the layered lanthanide aryl and alkyl phosphonates $\text{LnH}(\text{O}_3\text{PR})_2$ ($\text{Ln} = \text{Eu}, \text{Tb}$; $\text{R} = \text{CH}_3, \text{C}_2\text{H}_5, \text{C}_3\text{H}_7, \text{C}_6\text{H}_5$) exhibit interesting thermal stability up to 400 °C or 500 °C and intense luminescence with emission comparable to the $\text{Gd}_2\text{O}_2\text{S}:\text{Tb}$ commercial phosphor.^{7,8} Luminescence can be also enhanced by nanostructuring as shown for nanorods and dandelion-like particles of $\text{LnH}(\text{O}_3\text{PC}_6\text{H}_5)_2$ ($\text{Ln} = \text{Eu}, \text{Tb}$, Y:Eu, Y:Tb).^{9–11} Despite interesting luminescence properties, the $\text{LnH}(\text{O}_3\text{PC}_n\text{H}_{2n+2})_2$ hybrids have been less characterized,

particularly their crystal structures have not been detailed due to poor crystallization and systematic formation of twinned crystals. Indeed only the cell parameters and the space groups have been reported for the methyl phosphonate $\text{LaH}(\text{O}_3\text{PCH}_3)_2$.¹² In order to understand the influence of lanthanide ion environment on luminescence properties, we have reported herein the crystal structure of $\text{LaH}(\text{O}_3\text{PCH}_3)_2$ and photoluminescence properties of $\text{La}_{1-x}\text{Ln}_x\text{H}(\text{O}_3\text{PCH}_3)_2$ ($\text{Ln} = \text{Eu}, \text{Tb}$; $0 < x \leq 1$) doped hybrids.

2 Experimental

2.1 Synthesis and chemical analyses

The $\text{La}_{1-x}\text{Ln}_x\text{H}(\text{O}_3\text{PCH}_3)_2$ ($x = 0, 0.01, 0.05, 0.1, 0.2, 0.3, 0.5, 0.75, 1$; $\text{Ln} = \text{Eu}, \text{Tb}$) samples have been synthesized under hydrothermal conditions. Methyl phosphonic acid (80 mg, 0.83 mmol), $\text{La}(\text{NO}_3)_3 \cdot 6\text{H}_2\text{O}$ ($1 - x \times 0.415$ mmol), $\text{Ln}(\text{NO}_3)_3 \cdot 5\text{H}_2\text{O}$ ($x \times 0.415$ mmol) and urea (37.5 mg, 0.63 mmol) were dissolved in distilled water (15 mL). The resulting solutions were placed in a 23 mL PTFE vessel, introduced in a Berghof pressure digestion autoclave and heated from room temperature to 180 °C for 6 h, and at 180 °C for 24 h and finally cooled to room temperature in 24 h. The obtained mixtures were filtered, washed with distilled water and rinsed with absolute ethanol. The resulting powder samples were dried in air. %C and %H measured by elemental

^aLaboratoire CRISMAT, CNRS UMR6508, ENSICAEN, Université de Caen – Basse Normandie, 6 Bd Maréchal Juin, 14050 Caen Cedex, France.

E-mail: sophie.boudin@ensicaen.fr

^bLaboratoire CIMAP, CEA/CNRS UMR6252, ENSICAEN, Université de Caen – Basse Normandie, 6 Bd Maréchal Juin, 14050 Caen Cedex, France

^cUniversité Européenne de Bretagne, Université de Brest, CNRS UMR6521, CEMCA, Av. Victor Le Gorgeu, 29238 Brest, France

†Electronic supplementary information (ESI) available: S1: TGA curve of $\text{La}_{0.5}\text{Eu}_{0.5}\text{H}(\text{O}_3\text{PCH}_3)_2$, X-ray diffraction powder patterns of $\text{LaH}(\text{O}_3\text{PCH}_3)_2$, $\text{EuH}(\text{O}_3\text{PCH}_3)_2$ and $\text{TbH}(\text{O}_3\text{PCH}_3)_2$. S2: CIF of $\text{LaH}(\text{O}_3\text{PCH}_3)_2$. CCDC 1022572. For ESI and crystallographic data in CIF or other electronic format see DOI: 10.1039/c4dt02643h

analyses are in good agreement with the expected values with 7.01%C (calc. 7.18%) and 2.55%H (calc. 2.11%) for $\text{La}_{0.5}\text{Eu}_{0.5}\text{H}(\text{O}_3\text{PCH}_3)_2$, 6.53%C (calc. 7.05%) and 2.68%H (calc. 2.07%) for $\text{EuH}(\text{O}_3\text{PCH}_3)_2$, 6.47%C (calc. 7.11%) and 2.57%H (calc. 2.09%) for $\text{La}_{0.5}\text{Tb}_{0.5}\text{H}(\text{O}_3\text{PCH}_3)_2$, and 6.14%C (calc. 6.90%) and 2.60%H (calc. 2.03%) for $\text{TbH}(\text{O}_3\text{PCH}_3)_2$. Thermogravimetric analysis (TGA) of $\text{La}_{0.5}\text{Eu}_{0.5}\text{H}(\text{O}_3\text{PCH}_3)_2$ has been performed using a TGA 92 Setaram thermogravimetric analyser by heating under O_2 from 25 °C to 900 °C at $10^\circ \text{ min}^{-1}$, by keeping at 900 °C for 30 min and by cooling back to 25 °C. $\text{La}_{0.5}\text{Eu}_{0.5}\text{H}(\text{O}_3\text{PCH}_3)_2$ decomposes from 450 °C to 800 °C with $\text{La}_{0.5}\text{Eu}_{0.5}\text{PO}_4$ and $\text{La}_{0.5}\text{Eu}_{0.5}\text{P}_3\text{O}_9$ as the resulting products according to X-ray diffraction analysis. The total weight loss equal to 6.9% (calc. 6.9%) is in agreement with the reaction: $\text{La}_{0.5}\text{Eu}_{0.5}\text{H}(\text{O}_3\text{PCH}_3)_2 + 4\text{O}_2 \rightarrow \frac{1}{2}\text{La}_{0.5}\text{Eu}_{0.5}\text{PO}_4 + \frac{1}{2}\text{La}_{0.5}\text{Eu}_{0.5}\text{P}_3\text{O}_9 + 2\text{CO}_2 + 3.5\text{H}_2\text{O}$.

2.2 Powder X-ray diffraction

The powder X-ray diffraction patterns of $\text{La}_{1-x}\text{Ln}_x\text{H}(\text{O}_3\text{PCH}_3)_2$ ($0 \leq x \leq 1$; Ln = Eu, Tb) samples were recorded for $5^\circ \leq 2\theta \leq 90^\circ$ using a Panalytical X'pert Pro diffractometer with Cu K α ($\lambda_{\text{av}} = 1.5418 \text{ \AA}$) radiation. No impurity phases were detected.

2.3 Single crystal X-ray diffraction study

From the $\text{LaH}(\text{O}_3\text{PCH}_3)_2$ and $\text{La}_{0.5}\text{Tb}_{0.5}\text{H}(\text{O}_3\text{PCH}_3)_2$ samples, transparent single crystals were successfully isolated for single crystal X-ray diffraction study. In all the other samples, the crystals were too tiny to perform such studies. A $250 \mu\text{m} \times 150 \mu\text{m} \times 20 \mu\text{m}$ single crystal of $\text{LaH}(\text{O}_3\text{PCH}_3)_2$ with a good optical quality was selected from the $\text{LaH}(\text{O}_3\text{PCH}_3)_2$ sample using a stereomicroscope. A preliminary X-ray diffraction investigation was performed at room temperature, using Mo K α radiation on a Kappa CCD (Bruker Nonius) diffractometer equipped with an Apex2 CCD detector. Large Ω scans were used to control the crystalline quality of different samples and to determine cell parameters. The observation of a systematic lateral splitting of the reflections increasing with θ reveals the existence of twin domains. A suitable strategy was calculated to ensure complete data collection using the Apex2 suite, the cell parameters as well as details of the data collection are reported in ESI.† Two sets of reflections corresponding to two twin domains have been indexed and extracted separately. The twin domains are related to a two-fold axis parallel to **c** (pseudo merohedral twin). The intensities of the reflections were then integrated, scaled and corrected from the absorption using the empirical method implemented in TWINABS. A structural model considering the centro symmetric space group $P\bar{1}$ was built up with SUPERFLIP¹³ using the charge flipping method. The model was then introduced in the refinement program JANA2006,¹⁴ all the atomic positions and the anisotropic displacement parameters (ADP) were refined for all the atoms (except for the H atoms, for which the

Table 1 Positional parameters of $\text{LaH}(\text{O}_3\text{PCH}_3)_2$

Atom	x	y	z	u_{iso} (Å ²)
La1	0.2524(2)	0.26231(13)	0.46194(6)	0.0140(3)
P1	0.8887(4)	0.0622(3)	0.2977(2)	0.0141(6)
P2	−0.3652(4)	0.5750(3)	0.2973(2)	0.0134(6)
O1	0.0763(12)	0.1675(8)	0.2980(7)	0.020(2)
O2	−0.0242(11)	0.1387(8)	0.6747(7)	0.021(2)
O3	0.6732(11)	0.0717(8)	0.4087(7)	0.020(2)
O4	−0.1664(11)	0.4901(8)	0.4098(6)	0.0184(18)
O5	0.4501(12)	0.4679(8)	0.2966(7)	0.021(2)
O6	−0.5062(11)	0.7582(7)	0.3267(6)	0.0173(18)
C1	0.7368(16)	0.1326(13)	0.1370(9)	0.031(3)
C2	−0.2004(15)	0.6156(13)	0.1348(8)	0.028(3)
H1c1	0.8623	0.1017	0.0671	0.037(4)
H2c1	0.6007	0.0755	0.143	0.037(4)
H3c1	0.6652	0.2588	0.1142	0.037(4)
H1c2	−0.0677	0.6719	0.1386	0.033(4)
H2c2	−0.1231	0.5052	0.1116	0.033(4)
H3c2	−0.3213	0.6914	0.0662	0.033(4)
H1o2 ^a	−0.0959	0.2449	0.6601	0.025(3)
H1o6 ^a	−0.5801	0.8541	0.3421	0.021(3)

^a Site occupation = 0.5.

ADP values have been constrained equal to 1.2 times the ADP values of the adjacent C or O atoms). The twin ratios were refined to 64(5)% and 36(5)% for each domain. The Bond Valence Sum reveals a charge deficit on the O2 and O6 atoms, consequently the hydrogen atoms H1O2 and H1O6 were introduced close to these oxygen atoms. The position of the H atoms of the methyl groups and those linked to the oxygen atoms was determined on geometrical considerations. The final Fourier difference map does not show any presence of water molecules. The residual electronic density peaks, located very close to the La atom (at 1.1 Å), cannot correspond to oxygen atoms. Their high density values (up to $4.06 \text{ e}^- \text{ \AA}^{-3}$) can be explained by difficulties to refine the structural model due to the presence of twins. Atomic parameters and interatomic distances are summarized in Tables 1 and 2. Crystals of $\text{La}_{0.5}\text{Tb}_{0.5}\text{H}(\text{O}_3\text{PCH}_3)_2$ were selected for single crystal X-ray diffraction. They exhibit twin domains, cell parameters and the crystal structure similar to $\text{LaH}(\text{O}_3\text{PCH}_3)_2$ crystals. No La/Tb ordering has been detected.

Table 2 Interatomic distances of $\text{LaH}(\text{O}_3\text{PCH}_3)_2$ (Å). Symmetry codes: (i) $-x, -y + 1, -z + 1$; (ii) $-x + 1, -y, -z + 1$; (iii) $-x + 1, -y + 1, -z + 1$; (iv) $x + 1, y, z$; (v) $-x, -y, -z + 1$; (vi) $x - 1, y, z$

La1–O1	2.393(8)	P1–O1 ⁱⁱⁱ	1.498(8)
La1–O2	2.609(6)	P1–O2 ⁱ	1.550(6)
La1–O3	2.460(6)	P1–O3	1.526(6)
La1–O3 ⁱ	2.606(6)	P1–C1	1.776(9)
La1–O4	2.483(5)	P2–O4	1.528(6)
La1–O4 ⁱⁱ	2.602(7)	P2–O5 ^{iv}	1.497(8)
La1–O5	2.406(6)	P2–O6	1.566(6)
La1–O6 ⁱⁱ	2.607(7)	P2–C2	1.775(8)
O1–C1 ^{iv}	2.699(13)	O4–C2	2.696(10)
O2–C1 ⁱ	2.700(10)	O5–C2 ⁱⁱⁱ	2.677(11)
O3–C1	2.660(11)	O6–C2	2.707(11)
O2–H1o2	0.82	C1–H3c1	0.96
O6–H1o6	0.82	C2–H1c2	0.96
C1–H1c1	0.96	C2–H2c2	0.96
C1–H2c1	0.96	C2–H3c2	0.96

† Space group, cell parameters and agreement factors for $\text{LaH}(\text{O}_3\text{PCH}_3)_2$: $P\bar{1}$ (no. 2); $a = 5.3801(10) \text{ \AA}$; $b = 8.1410(15) \text{ \AA}$; $c = 10.1367(19) \text{ \AA}$; $\alpha = 73.807(8)^\circ$; $\beta = 83.716(8)^\circ$; $\gamma = 73.693(7)^\circ$; $V = 408.98(13) \text{ \AA}^3$; $R = 0.0473$; $R_w = 0.0591$.

2.4 Photoluminescence

The $\text{La}_{1-x}\text{Ln}_x\text{H}(\text{O}_3\text{PCH}_3)_2$ ($0 < x \leq 1$; Ln = Eu, Tb) Photo-Luminescence Excitation (PLE) and the PhotoLuminescence emission (PL) spectra have been measured every 1 nm at Room Temperature (RT) using a Horiba Jobin Yvon Fluorolog-3 spectrofluorimeter having a 450 W xenon lamp. Photoluminescence measurements have been performed on weighed powder, spread over a plate sample holder. Intensities measured for different samples, proportional to the emitting surfaces, were considered proportional to the volumes of samples, which are considered proportional to the masses of samples (the molar masses of $\text{La}_{1-x}\text{Ln}_x\text{H}(\text{O}_3\text{PCH}_3)_2$ varying only up to 6% with x and with Ln = Eu, Tb). Consequently, the measured intensities have been normalized for 1 g of the sample. The Commission Internationale de l'Eclairage (CIE) coordinates have been calculated using the chromatic functions published by Guild *et al.*¹⁵

3 Results and discussion

3.1 Structural description of $\text{LaH}(\text{O}_3\text{PCH}_3)_2$

The $\text{LaH}(\text{O}_3\text{PCH}_3)_2$ structure is composed of organic and inorganic layers alternating along c (Fig. 1). The organic layer is composed of a double sheet of protonated methyl phosphonate $\text{H}_{0.5}(\text{O}_3\text{PCH}_3)$ with methyl groups pointing inside the layer and with tetrahedral PO_3C phosphonate groups pointing outside the layer. The inorganic layer is composed of La^{3+} ions; each La^{3+} ion is surrounded by 8 oxygen atoms from phosphonate groups, forming a LaO_8 polyhedron. This polyhedron is formed from a LaO_5 pentagonal base with one oxygen atom above and two oxygen atoms below. Inside the inorganic layer, the LaO_8 polyhedra are connected by edges and form chains along the (110) direction (Fig. 2). The connection of the chains is ensured by the PO_3C groups in such a way that each PO_3C tetrahedron shares one edge of one LaO_8 polyhedron of one chain and one corner with one LaO_8 polyhedron

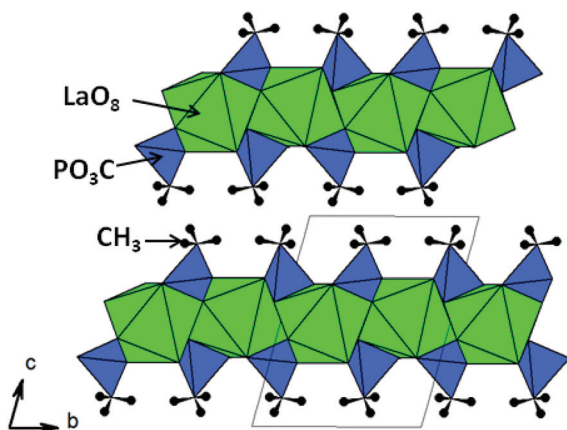


Fig. 1 Projection of $\text{LaH}(\text{O}_3\text{PCH}_3)_2$ along a . (The LaO_8 and PO_3C polyhedra are in green and blue, the methyl groups are represented with black balls and sticks.)

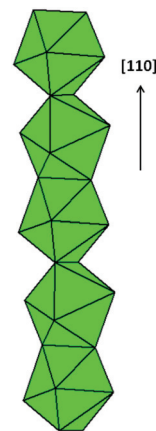


Fig. 2 The chain of LaO_8 polyhedra in $\text{LaH}(\text{O}_3\text{PCH}_3)_2$.

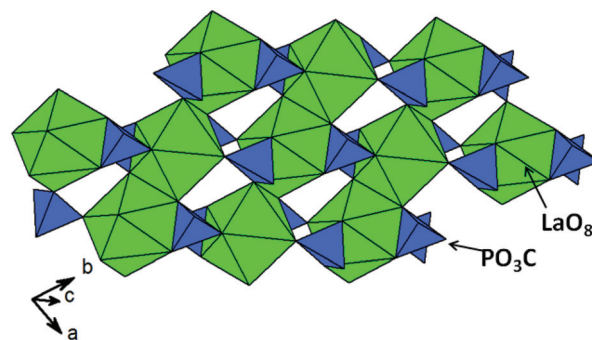


Fig. 3 Projection of the LaO_8 and PO_3C layer of $\text{LaH}(\text{O}_3\text{PCH}_3)_2$. (The LaO_8 and PO_3C polyhedra are in green and blue.)

of an adjacent chain (Fig. 3). Each LaO_8 polyhedron shares two edges with two PO_3C tetrahedra and four corners with four PO_3C tetrahedra. The structure of $\text{LaH}(\text{O}_3\text{PCH}_3)_2$ presents similarities with the $\text{LaH}(\text{O}_3\text{PC}_6\text{H}_5)_2$ one. Both structures are built up from organic and inorganic alternating layers. Within both types of inorganic layers: (i) the La^{3+} ions is eight coordinated with oxygen atoms from six PO_3C groups, (ii) the LaO_8 polyhedra share two opposite edges and form chains of LaO_8 polyhedra, (iii) each LaO_8 polyhedron is connected by two edges to two PO_3C groups, and by four corners to four PO_3C groups, (iv) the connection between the LaO_8 chain is ensured by the PO_3C groups, sharing one edge with one LaO_8 polyhedron from one chain and one corner with one LaO_8 polyhedron from an adjacent LaO_8 chain. In $\text{LaH}(\text{O}_3\text{PC}_6\text{H}_5)_2$, LaO_8 is a distorted dodecahedron with La–O distances ranging from 2.40(1) Å to 2.67(1) Å and in $\text{LaH}(\text{O}_3\text{PCH}_3)_2$, LaO_8 is a tri-capped pentagonal base, with La–O distances ranging from 2.393(8) Å to 2.607(7) Å.

3.2 Photoluminescence of $\text{La}_{1-x}\text{Eu}_x\text{H}(\text{O}_3\text{PCH}_3)_2$

The Room Temperature (RT) PhotoLuminescence Excitation (PLE) spectrum of $\text{EuH}(\text{O}_3\text{PCH}_3)_2$ recorded at $\lambda_{\text{em}} = 611$ nm is plotted in Fig. 4. It exhibits bands from 300 to 320 nm, 360 to 390 nm, 390 to 405 nm, at 415 nm, at 465 nm, from 525 to

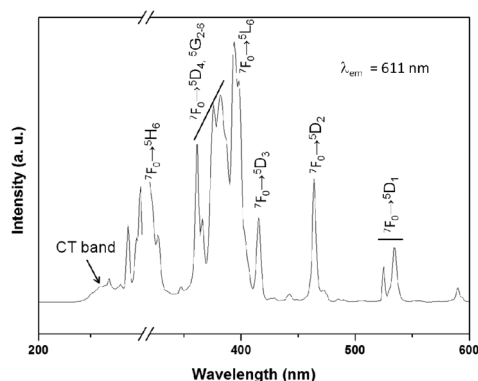


Fig. 4 The RT PLE spectrum of $\text{EuH}(\text{O}_3\text{PCH}_3)_2$ for $\lambda_{\text{em}} = 611$ nm.

540 nm ascribed to the ${}^7\text{F}_0 \rightarrow {}^5\text{H}_6$, ${}^7\text{F}_0 \rightarrow {}^5\text{D}_4$, ${}^5\text{G}_{2-6}$, ${}^7\text{F}_0 \rightarrow {}^5\text{L}_6$, ${}^7\text{F}_0 \rightarrow {}^5\text{D}_3$, ${}^7\text{F}_0 \rightarrow {}^5\text{D}_2$ and ${}^7\text{F}_0 \rightarrow {}^5\text{D}_1$ Eu^{3+} transitions, respectively.¹⁰ The maximum excitation band is observed for the ${}^7\text{F}_0 \rightarrow {}^5\text{L}_6$ transition at 394 nm (Fig. 5), it differs from the one reported by Rosa *et al.*⁷ for $\text{EuH}(\text{O}_3\text{PCH}_3)_2$, measured at 378 nm.

The RT PhotoLuminescence (PL) emission spectra of $\text{La}_{1-x}\text{Eu}_x\text{H}(\text{O}_3\text{PCH}_3)_2$ ($0 < x \leq 1$) recorded for $\lambda_{\text{exc}} = 394$ nm are plotted in Fig. 6. They exhibit bands at 580 nm, from 580 to 603 nm, 603 to 630 nm, 645 to 670 nm, 680 to 710 nm, ascribed to ${}^5\text{D}_0 \rightarrow {}^7\text{F}_0$, ${}^5\text{D}_0 \rightarrow {}^7\text{F}_1$, ${}^5\text{D}_0 \rightarrow {}^7\text{F}_2$, ${}^5\text{D}_0 \rightarrow {}^7\text{F}_3$ and ${}^5\text{D}_0 \rightarrow {}^7\text{F}_4$, respectively (Fig. 5). The single ${}^5\text{D}_0 \rightarrow {}^7\text{F}_0$ transition is in agreement with one single crystallographic $\text{La}^{3+}/\text{Eu}^{3+}$ site, moreover the high intensity ratio $I({}^5\text{D}_0 \rightarrow {}^7\text{F}_2)/I({}^5\text{D}_0 \rightarrow {}^7\text{F}_1)$ is in agreement with the fact that the Eu^{3+} ions lie on a general 2i position. The emission intensity increases with the Eu^{3+} doping rate as shown in Fig. 6 and Fig. 7, where the intensities integrated from 570 to 640 nm are plotted *versus* the Eu^{3+} doping rate. The maximum emission intensity is clearly observed for $\text{EuH}(\text{O}_3\text{PCH}_3)_2$ from 570 to 640 nm even though the maximal value of intensity at 611 nm is biased due to

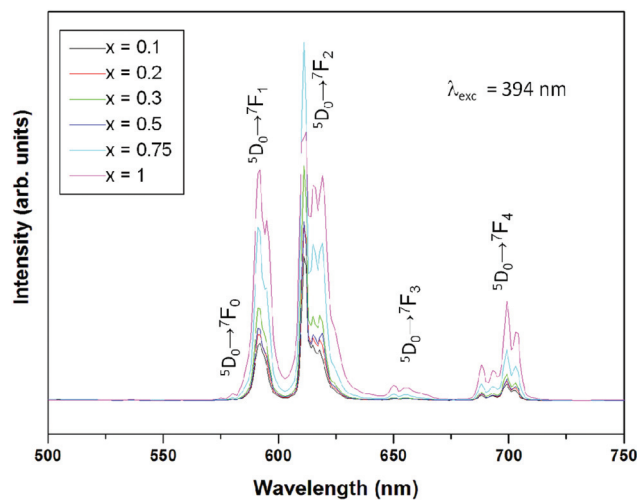


Fig. 6 RT PL spectra of $\text{La}_{1-x}\text{Eu}_x\text{H}(\text{O}_3\text{PCH}_3)_2$ recorded for $\lambda_{\text{exc}} = 394$ nm.

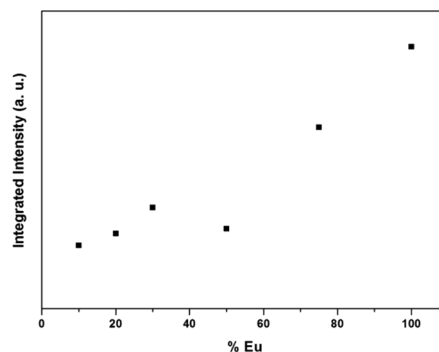


Fig. 7 Integrated intensity emitted between 570 nm and 640 nm for $\text{La}_{1-x}\text{Eu}_x\text{H}(\text{O}_3\text{PCH}_3)_2$ samples under $\lambda_{\text{exc}} = 394$ nm excitation.

detector saturation. No concentration quenching is observed and the maximum emission occurs for a critical concentration $x_c = 1$. Such result indicates that concentration quenching in $\text{La}_{1-x}\text{Eu}_x\text{H}(\text{O}_3\text{PCH}_3)_2$ occurs through a percolation model¹⁶ where x_c verifies the formula $x_c = 2/N$ with N being the number of the nearest neighbor Eu^{3+} ions around one Eu^{3+} ion. In $\text{EuH}(\text{O}_3\text{PCH}_3)_2$ where Eu^{3+} ions lie in the chains, N is equal to 2 and x_c to 1.

3.3 Photoluminescence of $\text{La}_{1-x}\text{Tb}_x\text{H}(\text{O}_3\text{PCH}_3)_2$

The PLE spectra of $\text{La}_{1-x}\text{Tb}_x\text{H}(\text{O}_3\text{PCH}_3)_2$ ($0 < x \leq 1$) recorded for $\lambda_{\text{em}} = 543$ nm are plotted in Fig. 8. They exhibit typical 4f–4f excitation bands of Tb^{3+} ions spread from 280 to 390 nm and from 475 to 500 nm. The most intense excitation band, centered at 378 nm, is assigned to the ${}^7\text{F}_6 \rightarrow {}^5\text{D}_3$ transition (Fig. 5). The spin allowed $4f^8 \rightarrow 4f^7 5d$ transition of Tb^{3+} , slightly larger than the 4f–4f transitions, can be observed between 250 nm and 265 nm within a wavelength range usually observed in oxides.¹⁷ The wavelength observed for the maximal intensity shifts slightly from 260 to 263 nm when the Tb^{3+} ratio varies from $x = 0.01$ to 1 as shown in the insert

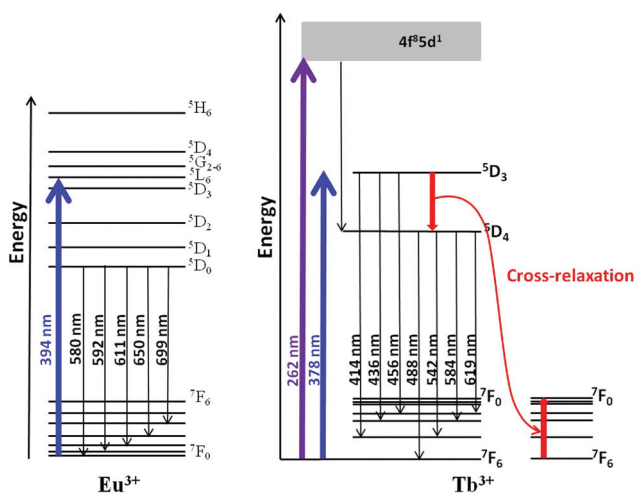


Fig. 5 Schema of excitation, relaxation and emission of Eu^{3+} and Tb^{3+} in $\text{La}_{1-x}\text{Ln}_x\text{H}(\text{O}_3\text{PCH}_3)_2$ ($\text{Ln} = \text{Eu}, \text{Tb}$).

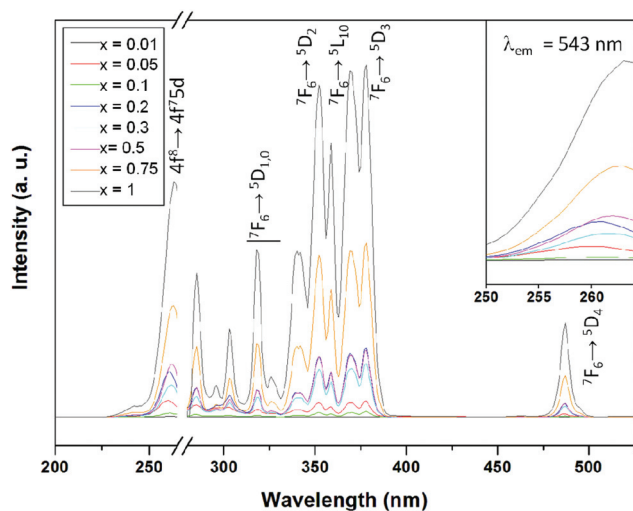


Fig. 8 RT PLE spectra of $\text{La}_{1-x}\text{Tb}_x\text{H}(\text{O}_3\text{PCH}_3)_2$ recorded for $\lambda_{\text{em}} = 543$ nm; the insert shows enlargement of the $4f^8 \rightarrow 4f^7 5d$ excitation band.

in Fig. 8. This subtle red shift is in agreement with the nephelauxetic effect expected when the Ln–O bonds become slightly more covalent when Tb^{3+} substitutes La^{3+} . In the present study the $4f^8 \rightarrow 4f^7 5d$ transition of Tb^{3+} is rather intense with excitation intensity equal to 2/3 of the $7F_6 \rightarrow 5D_3$ one. The spin forbidden $4f^8 \rightarrow 4f^7 5d$ transition of Tb^{3+} , expected at higher wavelength with a weaker emission¹⁷ compared to the spin allowed transition, is hidden by f–f transitions and cannot be observed. All the excitation intensities increase with the Tb^{3+} ratio. Note that the present $\text{TbH}(\text{O}_3\text{PCH}_3)_2$ PLE spectrum differs from the one reported by Rosa *et al.*^{7,8} where the $4f^8 \rightarrow 4f^7 5d$ transition is not observed.

The PL spectra of $\text{La}_{1-x}\text{Tb}_x\text{H}(\text{O}_3\text{PCH}_3)_2$ ($0 < x \leq 1$) recorded at the $4f\text{--}4f$ and $4f \rightarrow 4f 5d$ excitation band maxima, for $\lambda_{\text{exc}} = 378$ nm and $\lambda_{\text{exc}} = 262$ nm, respectively, are plotted in Fig. 9

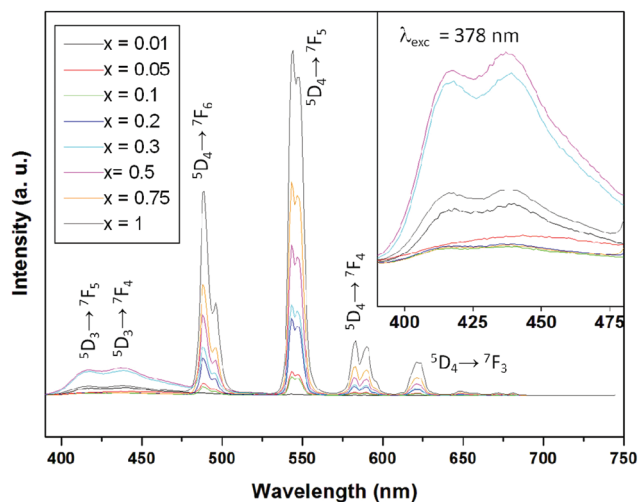


Fig. 9 RT PL spectra of $\text{La}_{1-x}\text{Tb}_x\text{H}(\text{O}_3\text{PCH}_3)_2$ recorded for $\lambda_{\text{exc}} = 378$ nm; the insert shows enlargement of the $5D_3 \rightarrow 7F_{5,4}$ emission band.

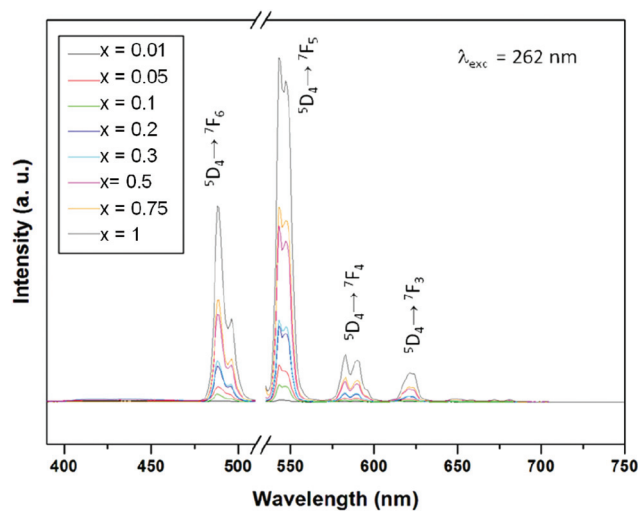


Fig. 10 RT PL spectra of $\text{La}_{1-x}\text{Tb}_x\text{H}(\text{O}_3\text{PCH}_3)_2$ recorded for $\lambda_{\text{exc}} = 262$ nm.

and 10. Emission bands from 400 to 425 nm, from 425 to 475 nm, from 475 to 510 nm, from 530 to 560 nm, from 575 to 600 nm and from 615 to 630 nm can be assigned to the $5D_3 \rightarrow 7F_{5,4}$, $5D_4 \rightarrow 7F_{6,5,4,3}$ transitions (Fig. 5). The green $5D_4 \rightarrow 7F_5$ emission band is the most intense one. Under 378 nm and 262 nm excitation wavelengths, the emission intensities of blue $5D_4 \rightarrow 7F_6$, green $5D_4 \rightarrow 7F_5$, orange $5D_4 \rightarrow 7F_4$ and red $5D_4 \rightarrow 7F_3$ transitions increase with the Tb^{3+} rate as shown on the PL spectra (Fig. 9 and 10) and on the curves of the integrated intensities of the green $5D_4 \rightarrow 7F_5$ transition (Fig. 11). Lack of concentration quenching in $\text{La}_{1-x}\text{Tb}_x\text{H}(\text{O}_3\text{PCH}_3)_2$ suggests energy migration through a percolation model as for Eu^{3+} doped samples. The blue $5D_3 \rightarrow 7F_{5,4}$ emission bands, between 400 nm and 475 nm, exhibit different behaviors. Under a 378 nm excitation wavelength, their intensities increase up to a Tb^{3+} rate of $x = 0.5$ and decrease for higher Tb^{3+} concentration as shown in the insert in Fig. 9.

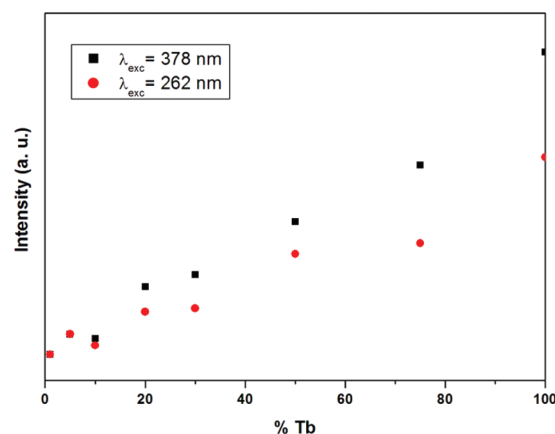


Fig. 11 RT emission intensity of $\text{La}_{1-x}\text{Tb}_x\text{H}(\text{O}_3\text{PCH}_3)_2$ integrated between 536 nm and 560 nm under 378 nm and 262 nm excitation wavelengths versus Tb^{3+} rate.

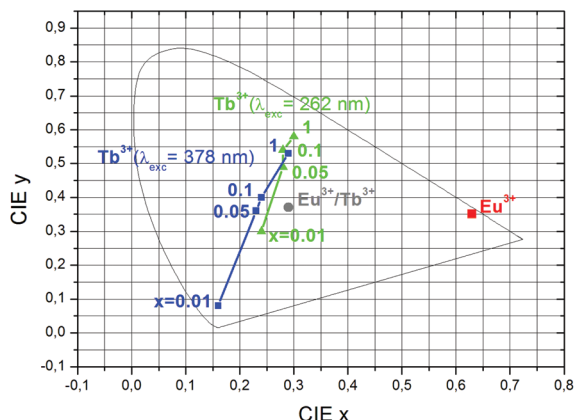


Fig. 12 CIE coordinates of $\text{La}_{1-x}\text{Ln}_x\text{H}(\text{O}_3\text{PCH}_3)_2$ ($\text{Ln} = \text{Tb}$; $x = 0.01, 0.05, 0.1, 1$; $\lambda_{\text{exc}} = 262$ nm and 378 nm: green and blue curves), ($\text{Ln} = \text{Eu}$; $0 < x \leq 1$; $\lambda_{\text{exc}} = 378$ nm: red square) and ($\text{Ln}_x = \text{Eu}_{0.03}\text{Tb}_{0.04}$; $\lambda_{\text{exc}} = 378$ nm: grey circle).

This feature can be explained by a cross relaxation phenomenon,¹⁸ in which the green emission from the $^5\text{D}_4$ level favored over the blue $^5\text{D}_3$ emission when the Tb^{3+} concentration increases (Fig. 5). Such a phenomenon results from joint $^5\text{D}_3 \rightarrow ^5\text{D}_4$ and $^7\text{F}_6 \rightarrow ^7\text{F}_0$ transitions between two closed Tb^{3+} ions. Under a 262 nm excitation wavelength, the blue $^5\text{D}_3 \rightarrow ^7\text{F}_{5,4}$ emission bands vanish, such a phenomenon can be explained by direct relaxation from the 4f5d level to the $^5\text{D}_4$ level of Tb^{3+} ions and emissions from this latter level to the $^7\text{F}_{6,5,4,3}$ ones (Fig. 5). Similar coupled 4f5d/ $^5\text{D}_4 \rightarrow ^7\text{F}_{6,5,4,3}$ relaxation/emissions have already been observed in phosphors like $\text{Y}_3\text{Ga}_5\text{O}_{12}:\text{Tb}$.¹⁹ Under a 378 nm excitation wavelength, relaxation from the $^5\text{D}_3$ levels and from the $^5\text{D}_4$ levels generate emission bands from 400 nm to 630 nm.

The PL spectra of $\text{La}_{1-x}\text{Tb}_x\text{H}(\text{O}_3\text{PCH}_3)_2$ clearly indicate that emission can be tuned from blue to green either by increasing the Tb^{3+} concentration *via* cross relaxation phenomenon or by turning the excitation wavelength from near UV (at 378 nm) to UV (at 262 nm). Fig. 12 shows the shifts of the CIE coordinates from blue ($x = 0.16, y = 0.08$) to green ($x = 0.29, y = 0.53$) as the Tb^{3+} doping rates vary from $x = 0.01$ to 1 under a 378 nm excitation wavelength and from blue ($x = 0.16, y = 0.08$) to cyan ($x = 0.24, y = 0.30$) as the $x = 0.01$ doped sample is irradiated by near UV (378 nm) or UV (262 nm) radiation.

4 Conclusion

The organic/inorganic $\text{La}_{1-x}\text{Ln}_x\text{H}(\text{O}_3\text{PCH}_3)_2$ ($\text{Ln} = \text{Eu}, \text{Tb}$) hybrids have been synthesized by hydrothermal synthesis. The crystal structure of $\text{LaH}(\text{O}_3\text{PCH}_3)_2$ consists of chains of edge-sharing LaO_8 polyhedra linked through PO_3C tetrahedra. The absence of concentration quenching in the Eu or Tb doped materials can be interpreted by energy migration through a percolation model. The photoemission of the Tb doped material can be adjusted by both the Tb rate and the excitation wavelength, from blue to cyan to green when the Tb rate

increases and from blue to cyan when the slightly Tb doped hybrid is exposed to near UV or UV. Since the red Eu and the blue/green Tb hybrids exhibit both large excitation bands at 378 nm, Eu/Tb co-doping has been investigated to synthesize a white phosphor. The slightly doped $\text{La}_{0.93}\text{Eu}_{0.03}\text{Tb}_{0.04}\text{H}(\text{O}_3\text{PCH}_3)_2$ material shows, under a 378 nm wavelength, a white/cyan emission with CIE coordinates ($x = 0.29; y = 0.37$) close to the white ($x = 0.33; y = 0.33$) emission (Fig. 12). It is thus an interesting candidate for white phosphor on a UV emitting diode. Moreover a $\text{EuH}(\text{O}_3\text{PCH}_3)_2/\text{TbH}(\text{O}_3\text{PCH}_3)_2$ mixture of fully substituted hybrids, deposited on a blue emitting InGaN diode, could be very interesting to generate a device with intense white emission. Compared to other white emitting organic/inorganic hybrids like $[\text{La}(1,3,5\text{-benzenetricarboxylate})] \cdot (\text{H}_2\text{O})_6$; Eu, Tb,²⁰ $[\text{Ln}(\text{benzimidazole-5,6-dicarboxylate})_4(1,10\text{-phenanthroline})_2(\text{NO}_3)] \cdot 2\text{H}_2\text{O}$ ($\text{Ln} = \text{Gd}, \text{Eu}, \text{Tb}$)²¹ or $[\text{Zn}_3(1,3,5\text{-tri}(4\text{-carboxyphenoxy})\text{benzene})_2(\text{H}_2\text{O})_2] \cdot 2\text{H}_2\text{O} \cdot 4\text{DMF}$: Tb, Eu,²² $\text{La}_{1-x}\text{Ln}_x\text{H}(\text{O}_3\text{PCH}_3)_2$ hybrids offer several advantages in one material. Indeed (i) because they are water free, they are highly stable (up to 450 °C), (ii) made from the very cheap organic precursor methylphosphonic acid, they can be used for low cost devices and (iii) they can be heavily doped to produce intense emission.

Acknowledgements

The authors acknowledge the financial support of the French Agence Nationale de la Recherche (ANR), through the program "Investissements d'Avenir"(ANR-10-LABX-09-01), Labex EMC³.

Notes and references

- G. Cao, H. G. Hong and T. E. Mallouk, *Acc. Chem. Res.*, 1992, **25**, 420–427.
- M. E. Thompson, *Chem. Mater.*, 1994, **6**, 1168–1175.
- H. E. Katz, *Chem. Mater.*, 1994, **6**, 2227–2232.
- A. Clearfield, *Curr. Opin. Solid State Mater. Sci.*, 1996, **1**, 268–278.
- A. Clerafield, *Prog. Inorg. Chem.*, 1998, **47**, 371.
- J. G. Mao, *Coord. Chem. Rev.*, 2007, **251**, 1493–1520.
- I. L. V. Rosa, E. J. Nassar and O. A. Serra, *J. Alloys Compd.*, 1998, **275–277**, 315–317.
- I. L. V. Rosa, A. V. Santos de Lourenço, C. R. Neri and O. A. Serra, *J. Fluoresc.*, 2006, **16**, 455–459.
- S. Y. Song, J. F. Ma, J. Yang, M. H. Cao, H. J. Zhang, H. S. Wang and K. Y. Yang, *Inorg. Chem.*, 2006, **45**, 1201–1207.
- W. Di, R. A. S. Ferreira, M. G. Willinger, X. Ren and N. Pinna, *J. Phys. Chem. C*, 2010, **114**, 6290–6297.
- W. Di, X. Ren, N. Shirahata, C. Liu, L. Zhang, Y. Sakka and N. Pinna, *CrystEngComm*, 2011, **13**, 5226–5233.
- G. Cao, V. M. Lynch, J. S. Swinnea and T. E. Mallouk, *Inorg. Chem.*, 1990, **29**, 2112–2117.

- 13 L. Palatinus and G. Chapuis, *J. Appl. Crystallogr.*, 2007, **40**, 786–790.
- 14 V. Petricek, M. Dusek and L. Palatinus, *Jana2006. Structure Determination Software Programs*, Institute of Physics, Praha, Czech Republic, 2006.
- 15 J. Guild, *Philos. Trans. R. Soc. London, A*, 1931, **230**, 149–187.
- 16 P. A. M. Berdowski and G. Blasse, *J. Solid State Chem.*, 1986, **63**, 86–88.
- 17 P. Dorenbos, *J. Lumin.*, 2000, **91**, 91–106.
- 18 Z. Hao, J. Zhang, X. Zhang, S. Lu and X. Wang, *J. Electrochem. Soc.*, 2009, **156**(3), H193–H196.
- 19 N. Zhu, Y. Li, X. Yu and W. Ge, *J. Lumin.*, 2007, **122–123**, 704–706.
- 20 K. Liu, H. You, Y. Zheng, G. Jia, Y. Huang, M. Yang, Y. Song, L. Zhang and H. Zhang, *Cryst. Growth Des.*, 2010, **10**, 16–19.
- 21 X. Ma, X. Li, Y. E. Cha and L. P. Jin, *Cryst. Growth Des.*, 2012, **12**, 5227–5232.
- 22 H. He, F. Sun, T. Borjigin, N. Zhao and G. Zhu, *Dalton Trans.*, 2014, **43**, 3716–3721.